

Temporally Coherent Imitation Learning via Latent Action Flow Matching for Robotic Manipulation

Wu Songwei, Jiang Zhiduo, Xie Guanghu, Liu Yang[†], Liu Hong

Abstract—Learning long-horizon robotic manipulation requires jointly achieving expressive behavior modeling, real-time inference, and stable execution, which remains challenging for existing generative policies. Diffusion-based approaches offer strong modeling capacity but incur high inference latency, while flow matching enables fast one-step generation yet often suffers from unstable execution when operating directly in the raw action space. We propose **LG-Flow Policy**, a trajectory-level imitation learning framework that performs flow matching in a continuous latent action space. By encoding action sequences into temporally regularized latent trajectories and learning an explicit latent-space flow, **LG-Flow Policy** decouples global motion structure from low-level control noise, enabling smooth and reliable long-horizon execution. The framework further integrates geometry-aware point cloud conditioning and execution-time multimodal modulation, with visual cues as a representative modality evaluated in real-world settings for robust deployment. Experiments in simulation and on real robots show that **LG-Flow Policy** achieves near single-step inference, improves trajectory smoothness by up to 93.7% and task success by up to 25% over raw action-space flow baselines, while remaining significantly faster than diffusion-based policies.

Index Terms—Imitation learning, flow-based policy, real-time robot control, trajectory generation

I. INTRODUCTION

Diffusion-based policies (DP) [1] have demonstrated strong performance in robotic visuomotor imitation learning, particularly for complex manipulation tasks in both simulation and real-world environments. By modeling multimodal action distributions conditioned on rich sensory observations such as images [1], [2] or point clouds [3]–[5], these methods enable expressive behavior modeling and generalization across diverse task variations.

More recently, flow matching [6]–[8] has emerged as an alternative generative paradigm for robotic control [9]–[11]. By formulating action generation as the solution of an ordinary differential equation (ODE), flow matching enables near one-step inference and substantially improves inference efficiency compared to diffusion-based approaches, making it a promising framework for real-time imitation learning.

Despite these advances, deploying generative policies on physical robots remains challenging. Diffusion policies rely on iterative denoising, which introduces nontrivial inference

latency and limits real-time applicability. Flow matching methods, while efficient, generate trajectories directly in the raw action space, where modeling noise and numerical errors tend to accumulate over long horizons, resulting in jittery trajectories and degraded execution stability. As a result, existing approaches struggle to simultaneously achieve expressive behavior modeling, fast inference, and stable execution.

Several recent works have explored different strategies to alleviate these issues. DP3 [3] and iDP3 [12] improve perception efficiency through lightweight point cloud encoders, RDP [13] introduces a hierarchical Fast–Slow control structure for long-horizon behaviors, and Flow Policy [9] incorporates consistency constraints to enhance execution performance. However, our experimental results indicate that the fundamental trade-off between inference efficiency and execution stability has not yet been fully resolved.

To address this challenge, we propose **LG-Flow Policy**, a trajectory-level action generation framework that performs flow matching in a continuous latent action space. By mapping action sequences into temporally regularized latent trajectory representations and learning an explicit latent-space flow, **LG-Flow Policy** preserves the inference efficiency of flow-based methods while substantially improving execution smoothness and stability. Operating on motion-level latent representations decouples global trajectory structure from low-level control noise, mitigating error amplification during trajectory generation and enabling more reliable long-horizon behaviors.

LG-Flow Policy further integrates geometry-aware point cloud conditioning and execution-time visual modulation from a wrist-mounted camera, providing rich environmental awareness without perturbing latent trajectory dynamics. Extensive simulation and real-world experiments demonstrate that the proposed approach consistently achieves smooth trajectories, high task success rates, and fast response times, outperforming both diffusion-based and raw action-space flow-based baselines.

Our main contributions are summarized as follows:

- We introduce a trajectory-level latent flow matching framework that reconciles fast inference with smooth and stable robotic manipulation.
- We show that performing flow matching in a continuous latent action space significantly reduces trajectory jitter and improves execution reliability.
- We demonstrate through comprehensive simulation and real-world experiments that the proposed method achieves robust performance across diverse tasks, including improved tolerance to heterogeneous and suboptimal demonstrations.

[†]Corresponding author: Liu Yang (liuyanghit@hit.edu.cn).

*This work was supported by the Natural Science Foundation of Heilongjiang Province for Excellent Young Scholars (Grant No. YQ2024E018) and the Youth Talent Support Program of the China (Grant No. 2022-JCJQQT-061).

All authors are with the State Key Laboratory of Robotics and Systems, Harbin Institute of Technology, Harbin 150001, Heilongjiang, China

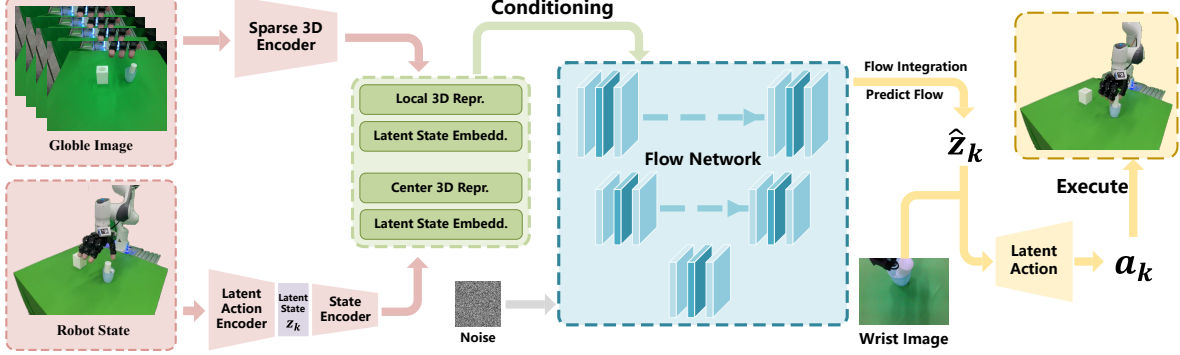


Fig. 1. Overall architecture of the proposed LG-Flow Policy. The system first encodes point cloud observations into geometry-aware scene features, then performs latent-space flow matching to generate temporally coherent latent action trajectories, which are finally decoded into executable control commands under visual conditioning.

II. RELATED WORK

A. Diffusion and Flow-Based Policies for Robotics

Diffusion-based policies [1]–[3], [5], [12], [14] model vi suomotor control as conditional trajectory generation and achieve strong performance in complex manipulation tasks. However, their reliance on iterative denoising leads to high inference latency and sensitivity to execution noise, limiting real-time deployment. Acceleration strategies such as DDIM [15] or hierarchical designs like RDP [13] alleviate but do not eliminate the need for multi-step inference, leaving the recursive nature of diffusion a fundamental bottleneck.

Flow-based generative models [6], [7] provide a more direct alternative by learning vector fields that define probability paths via ODEs. Flow Matching enables fast inference by directly regressing velocity fields, and recent consistency-based variants [9]–[11] further reduce sampling steps. Despite their efficiency, flow-based policies often exhibit trajectory oscillations when applied directly in raw action spaces, especially under high-dimensional actions and complex visual inputs.

Our work builds on consistency flow matching while addressing this limitation through trajectory-level latent modeling and geometry-aware conditioning.

B. Visual Imitation Learning with 3D Representations

Early visual imitation learning methods rely primarily on 2D image observations [1], [16], processed by convolutional networks [17] or vision transformers [18]. Recent 3D-based approaches [3], [4], [12], [19] incorporate depth or point clouds and improve geometric reasoning, but commonly face two challenges.

First, prediction-and-planning formulations [20], [21] estimate 3D keyframes or target poses, introducing additional optimization at test time and scaling poorly to high-dimensional control. Second, efficient point cloud encoding remains difficult: PointNet-style architectures [22] can be computationally expensive [4], while simplified encoders [3], [12] trade geometric sensitivity for speed.

In contrast, our work follows a policy-centric design that directly outputs continuous actions, integrating structured 3D

geometric representations while maintaining real-time-capable inference.

C. Trajectory-Level Modeling and Dexterous Manipulation

Dexterous manipulation has traditionally been addressed using reinforcement learning or task-specific pipelines [21], [23], often requiring extensive training or carefully engineered structures. Recent imitation learning methods model action sequences or chunks [1], [9], but may still suffer from temporal inconsistency under long-horizon, high-dimensional control.

Trajectory-level modeling improves long-horizon coherence and robustness to noisy or suboptimal demonstrations, with latent action representation playing a central role. Discrete latents via VQ-VAE [24] are widely adopted [25]–[27] to enforce information bottlenecks, but may limit expressiveness. Recent studies show that appropriately structured continuous latent representations can achieve strong performance without sacrificing stability [28], [29]. For example, CoMo [30] mitigates shortcut learning through temporal difference modeling, and LAOM [31] demonstrates the benefits of higher-capacity continuous bottlenecks.

These results motivate trajectory-level continuous latent action modeling as an effective mechanism for generating smooth and temporally coherent dexterous behaviors, which we adopt in this work.

III. METHODS

A. Coherent Latent Action Representation

Long-horizon robotic manipulation requires action trajectories that are both expressive and execution-stable. Applying flow-based generative models directly in the raw action space often amplifies high-frequency noise during trajectory integration, leading to jittery and unreliable behaviors. To address this issue at its source, we introduce a *trajectory-level continuous latent action representation* that explicitly regularizes the geometry of the generation space before flow matching is applied. The overall architecture is illustrated in Fig. 2.

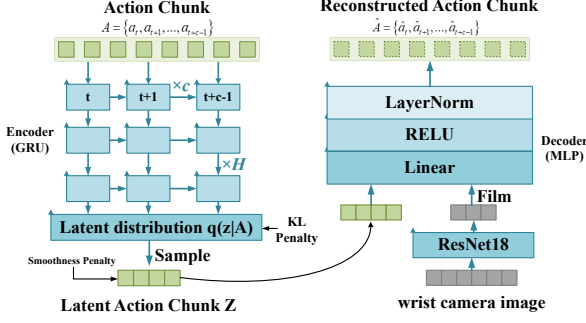


Fig. 2. Conditional variational autoencoder for latent action modeling. A GRU encoder enforces temporal coherence in the latent space, while an MLP decoder with FiLM-conditioned wrist-camera features enables visually adaptive action execution.

a) Trajectory-Level Latent Modeling: Instead of modeling individual control commands, we encode short-horizon action segments into latent variables that represent motion-level abstractions. Given an action trajectory $\mathbf{A}_{t:t+H-1} \in \mathbb{R}^{H \times d_a}$, we divide it into K consecutive chunks $\{\mathbf{A}^{(1)}, \dots, \mathbf{A}^{(K)}\}$, each spanning c time steps. Each chunk is mapped to a compact feature embedding and processed by a recurrent encoder with gated memory. Specifically, we employ a GRU-based encoder to aggregate action chunks over time,

$$\mathbf{h}_k = \text{GRU}(\mathbf{x}_k, \mathbf{h}_{k-1}), \quad (1)$$

where \mathbf{x}_k denotes the feature embedding of the k -th action chunk, obtained via a lightweight temporal convolution.

The recurrent structure plays a critical role in shaping the latent space. By conditioning each latent code on the entire history of preceding action segments, the GRU introduces a strong temporal inductive bias that suppresses high-frequency variations and enforces trajectory-level coherence. As a result, the latent space forms a smooth trajectory manifold rather than a collection of independent step-level representations, which is particularly beneficial for stabilizing downstream ODE-based flow matching. Empirically, we observe that replacing the recurrent encoder with non-recurrent, per-chunk independent encoders leads to noticeably increased trajectory jitter.

b) Variational Regularization: To further regularize the latent action space, we adopt a variational formulation. The KL divergence between the posterior and a standard normal prior encourages compactness and continuity of the latent distribution, improving robustness to noisy or suboptimal demonstrations. Importantly, this regularization operates at the trajectory level rather than the control-step level, making it well suited for long-horizon manipulation.

c) Visual-Conditioned Action Decoding: The proposed decoding mechanism is designed to flexibly incorporate execution-time sensory information without interfering with latent trajectory generation. In principle, when available, diverse modalities (e.g., vision, touch, and language) can be incorporated into the decoder through FiLM, enabling flexible multimodal conditioning while preserving coherent latent trajectory dynamics. Since the decoder operates at low computational cost, incorporating additional conditioning signals

at this stage allows the policy to leverage richer information without sacrificing real-time responsiveness.

In this work, we instantiate this design using wrist-mounted camera observations in real-world experiments. Specifically, images captured at execution time are processed by a lightweight visual encoder, and the resulting features are used to modulate the decoder through FiLM layers. Given a latent action code \mathbf{z}_k , the decoder reconstructs the corresponding action chunk as

$$\hat{\mathbf{A}}^{(k)} = f\theta(\mathbf{z}_k \mid \mathbf{v}_t), \quad (2)$$

where \mathbf{v}_t denotes the encoded visual feature. By confining perceptual conditioning to the decoding stage, the system cleanly separates latent trajectory planning from execution-time adaptation, allowing low-level action realization to react to scene variations while maintaining the smoothness and temporal coherence of the latent plan.

d) Training Objective: The latent action representation is trained using a standard variational objective with a reconstruction term and a KL regularizer, augmented by a lightweight smoothness constraint between consecutive latent codes. While the smoothness term serves as an auxiliary regularizer, the primary source of temporal coherence arises from the recurrent encoding structure itself.

Overall, the proposed representation defines a low-dimensional, continuous, and temporally regularized latent action space. By reshaping the generation manifold prior to flow matching, it lays the foundation for stable and efficient long-horizon trajectory generation, which we describe next.

B. Latent-Space Action Generation via Flow Matching

Given a sequence of latent action codes $\{\mathbf{z}_1, \dots, \mathbf{z}_K\}$ obtained from the trajectory-level encoder, we generate long-horizon manipulation behaviors by modeling their evolution in continuous time using flow matching. Unlike diffusion-based policies that rely on iterative denoising, flow matching enables efficient one-step generation. However, when applied directly in the raw action space, flow-based models are highly sensitive to local inconsistencies and noise. We therefore perform flow matching exclusively in the regularized latent action space, which is explicitly designed to be smooth and temporally coherent (Sec. III-A).

a) Latent-Space Flow Dynamics: Let \mathbf{z} denote a latent action code sampled from the target latent distribution and $\tilde{\mathbf{z}}$ a corresponding sample from a simple base distribution. We learn a time-dependent vector field $\boldsymbol{\nu}_\theta(t, \mathbf{z})$ that defines a continuous probability path from the source to the target distribution, governed by the ordinary differential equation

$$\frac{d\xi_{\mathbf{z}}(t)}{dt} = \boldsymbol{\nu}_\theta(t, \xi_{\mathbf{z}}(t)), \quad \xi_{\mathbf{z}}(0) = \tilde{\mathbf{z}}. \quad (3)$$

Operating on motion-level latent representations rather than raw control signals substantially improves numerical stability, as the smooth geometry of the latent space suppresses the amplification of high-frequency variations during trajectory generation.

b) Consistency Flow Matching in Latent Space: To efficiently learn the latent vector field across noise levels, we adopt consistency flow matching (CFM) and define the flow function

$$f_\theta(t, \mathbf{z}) = \mathbf{z} + (1-t) \boldsymbol{\nu}_\theta(t, \mathbf{z}), \quad (4)$$

where $t \in [0, 1]$ interpolates between the source and target latent distributions. Here, $\boldsymbol{\nu}_\theta(t, \mathbf{z})$ represents a learned velocity field in the latent action space, and the factor $(1-t)$ attenuates update magnitudes as the trajectory approaches the target distribution, improving stability near convergence. We further apply a time-dependent input normalization

$$c_{\text{in}}(t) = \frac{1}{\sqrt{t^2 + (1-t)^2}}, \quad (5)$$

to balance latent state scales across the time horizon.

c) One-Step Latent Trajectory Generation: At inference time, latent action codes are sampled from the base distribution and transformed via a single evaluation of the learned flow:

$$\tilde{\mathbf{z}}_k = f_\theta(1, \tilde{\mathbf{z}}_k). \quad (6)$$

In contrast to diffusion-based policies that require iterative denoising through multiple inference steps, our approach learns an explicit latent-space flow field during training and therefore performs single-step integration at test time. This enables one-shot generation of the entire latent action trajectory without iterative sampling or numerical integration loops, substantially reducing inference latency.

The resulting latent trajectory preserves temporal coherence by construction and is decoded into executable action segments using the visual-conditioned decoder described in Sec. III-A. By decoupling trajectory generation from execution-level adaptation, the policy achieves both fast inference and stable, smooth manipulation behavior.

C. Geometry-Aware 3D Scene Conditioning

Stable execution of latent action trajectories requires accurate awareness of scene geometry, as geometric errors can propagate across multiple decoded action segments over long horizons. We therefore condition the latent flow policy on a compact, geometry-aware 3D scene representation derived from point clouds.

a) Point Cloud Encoding: Scene point clouds are reconstructed from depth images captured by a fixed global camera, followed by workspace cropping to remove irrelevant background. Farthest Point Sampling (FPS) is applied to select a sparse set of center points that uniformly cover the workspace, serving as anchors for local neighborhood construction.

To capture geometric information at multiple spatial scales, we adopt a dual-branch encoder consisting of a local encoder f_l and a center encoder f_c , whose overall architecture is illustrated in Fig. 3. The local encoder aggregates relative point offsets within each neighborhood using a residual convolutional backbone with combined max-mean pooling, focusing on contact-level geometry that is invariant to global translation. In parallel, the center encoder maps the sampled center coordinates to a compact global context vector via a

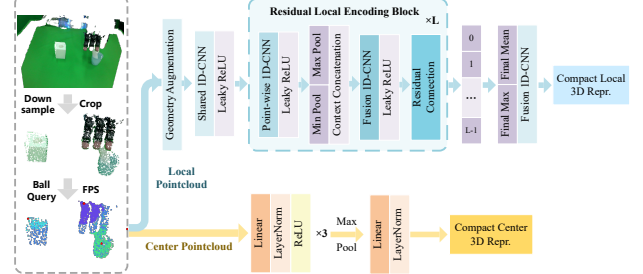


Fig. 3. Geometry-aware point cloud encoder. Local neighborhoods around farthest-sampled centers capture translation-invariant local geometry via residual convolutions and max-mean pooling, while a lightweight center encoder provides compact global scene context for latent trajectory conditioning.

lightweight MLP, capturing coarse scene layout with minimal computational overhead:

$$\mathbf{f}_l = f_l(\mathbf{pcd}_{\text{local}}), \quad \mathbf{f}_c = f_c(\mathbf{pcd}_{\text{center}}). \quad (7)$$

b) Hierarchical Geometric Conditioning: The extracted geometric features are injected into the latent flow network through a two-stage feature-wise linear modulation (FiLM) mechanism. Given an intermediate activation \mathbf{h} , local geometric modulation is applied first, followed by center-level conditioning:

$$\mathbf{h}' = \boldsymbol{\gamma}_l \odot \mathbf{h} + \boldsymbol{\beta}_l, \quad [\boldsymbol{\gamma}_l, \boldsymbol{\beta}_l] = \text{MLP}_l(\mathbf{f}_l), \quad (8)$$

$$\mathbf{h}'' = \boldsymbol{\gamma}_c \odot \mathbf{h}' + \boldsymbol{\beta}_c, \quad [\boldsymbol{\gamma}_c, \boldsymbol{\beta}_c] = \text{MLP}_c(\mathbf{f}_c). \quad (9)$$

Applying local modulation prior to center-level conditioning allows the policy to first adapt to contact-level constraints and subsequently adjust according to global scene structure, which we find to be more effective than the reverse ordering.

Overall, this geometry-aware conditioning provides the latent action model with robust spatial context, enabling stable long-horizon manipulation without compromising inference efficiency.

IV. EXPERIMENTS

A. Evaluation Metrics

We evaluate all methods using three complementary metrics that jointly characterize task performance, real-time efficiency, and execution quality: task success rate, response time, and trajectory smoothness.

a) Task Success Rate.: Task success rate is defined as the percentage of trials that satisfy task-specific success criteria within the episode horizon. Success is determined by predefined geometric constraints, including object pose errors below threshold and stable grasps or placements maintained for a minimum duration.

b) Response Time.: Response time measures the end-to-end inference latency from receiving sensory observations to outputting control actions, reflecting the real-time computational efficiency and closed-loop responsiveness of each policy.

TABLE I

MAIN RESULTS FOR SIMULATION EXPERIMENTS. SUCCESS RATES (%) ARE REPORTED AS MEAN \pm STANDARD DEVIATION. AVG. SUCCESS RATE AVERAGES RESULTS OVER ADROIT AND METAORLD. Δ SUCCESS / Δ TIME DENOTE RELATIVE CHANGES W.R.T. DP3 (BASELINE) IN AVERAGE SUCCESS RATE AND PER-STEP INFERENCE LATENCY.

Methods	Success rate in Adroit	Success rate in MetaWorld	Avg. Success rate	Δ Success	Avg. Time	Δ Time
Diffusion Policy	26.0 ± 4.0	37.3 ± 2.3	31.7 ± 6.9	-34.0	35.7 ms	-20.2
Flow Policy	56.7 ± 2.3	65.3 ± 2.3	61.0 ± 5.2	-4.7	6.1 ms	-49.8
DP3 (Baseline)	62.0 ± 2.0	69.3 ± 3.1	65.7 ± 4.6	0.0	55.9 ms	0.0
iDP3	62.7 ± 2.3	71.3 ± 2.3	67.0 ± 5.2	+1.3	58.9 ms	+3.0
RDP	70.0 ± 2.0	76.0 ± 2.0	73.0 ± 3.7	+7.3	57.3 ms	+1.4
LG-Flow Policy (Ours)	76.0 ± 2.0	80.7 ± 3.1	78.3 ± 3.4	+12.6	7.5 ms	-48.4

c) *Trajectory Smoothness*.: To quantify long-horizon execution stability, we define a trajectory smoothness metric that captures both time-domain and frequency-domain characteristics of executed joint trajectories. Specifically, smoothness is computed as a weighted combination of discrete-time jerk and high-frequency spectral energy.

Given a sequence of joint actions $\{\mathbf{a}_t\}_{t=1}^T$ with control timestep Δt , jerk is approximated using a third-order finite difference:

$$\mathbf{j}_t = \frac{\mathbf{a}_{t+1} - 3\mathbf{a}_t + 3\mathbf{a}_{t-1} - \mathbf{a}_{t-2}}{(\Delta t)^3}. \quad (10)$$

The time-domain smoothness term is defined as the mean squared jerk magnitude:

$$\mathcal{S}_{\text{jerk}} = \frac{1}{T-2} \sum_{t=3}^T \|\mathbf{j}_t\|_2^2. \quad (11)$$

To further capture high-frequency oscillations not fully reflected by jerk alone, we compute the frequency-domain energy of each joint trajectory using the discrete Fourier transform (DFT). Let $\hat{\mathbf{a}}_f$ denote the Fourier coefficients of $\{\mathbf{a}_t\}$. The high-frequency energy ratio is defined as

$$\mathcal{S}_{\text{freq}} = \frac{\sum_{f > f_c} \|\hat{\mathbf{a}}_f\|_2^2}{\sum_f \|\hat{\mathbf{a}}_f\|_2^2}, \quad (12)$$

where f_c is a cutoff frequency separating low- and high-frequency components.

The final trajectory smoothness metric is given by

$$\mathcal{S}_{\text{smooth}} = \alpha \mathcal{S}_{\text{jerk}} + \beta \mathcal{S}_{\text{freq}}, \quad (13)$$

where lower values indicate smoother trajectories with reduced abrupt variations and high-frequency oscillations. Based on extensive empirical evaluation and normalization of the two terms, we set $\alpha = 0.25$ and $\beta = 0.75$ in all experiments.

B. Simulation Experiments

1) Simulation Setup:

a) *Simulation Benchmarks*.: We evaluate all methods on two widely used manipulation benchmarks, Adroit [32] and Meta-World [33], covering 37 tasks in total. Adroit focuses on contact-rich dexterous manipulation with a high-dimensional articulated hand, while Meta-World consists of diverse arm-based manipulation tasks with varying difficulty. Both benchmarks are built upon the MuJoCo [34] physics simulator. For both benchmarks, expert demonstrations are collected using well-tuned heuristic policies to ensure consistent data quality.

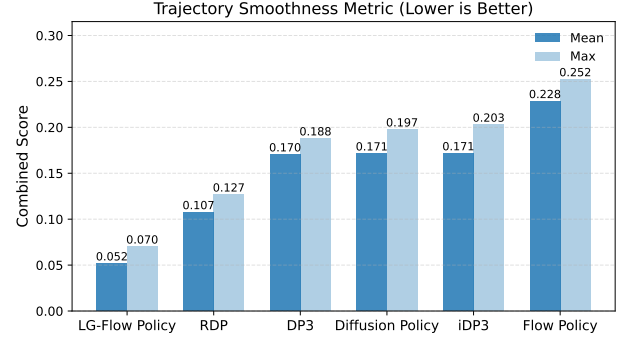


Fig. 4. Trajectory smoothness comparison across simulated manipulation tasks. Lower values indicate smoother execution.

b) *Baselines*.: We compare our method against representative diffusion- and flow-based visuomotor policies. DP3 [3] serves as the primary point-cloud-based diffusion baseline, with iDP3 [12] and Reactive Diffusion Policy (RDP [13]) included as advanced variants. Due to environment constraints, RDP is evaluated without force or pressure sensing, and employs a standard VAE as a latent-space encoder on top of DP. We further include a 2D RGB-based Diffusion Policy [1] and a standard Flow Policy [9] to contrast 3D conditioning and latent-space modeling.

c) *Training and Implementation Details*.: All methods condition on the two most recent observations and predict actions for the subsequent four steps. For each task, 30 expert demonstrations are collected, and performance is evaluated over 50 rollouts. RGB observations are cropped to 84×84 , and point clouds are downsampled using farthest point sampling to 512 points. Models are trained for 150 epochs using AdamW with a learning rate of 1×10^{-4} , batch size 96, and EMA with decay rate 0.95. State and action inputs are normalized to $[-1, 1]$, with actions unnormalized before execution. All experiments are conducted on identical hardware with an Intel Core i7-14700KF CPU and an NVIDIA RTX 4090D GPU. In simulation, no additional execution-time sensory signals are provided to the decoder, and action decoding relies solely on the latent action representation.

2) *Simulation Results Analysis*: Simulation results are evaluated from three perspectives: trajectory smoothness, inference latency and task success.

a) *Trajectory Smoothness*.: Fig. 4 reports trajectory smoothness across all simulated tasks. LG-Flow Policy



Fig. 5. Real-world experimental setup and observations. Left: Franka Emika Panda robot with a LEAP Hand and the visual sensing setup (global L515 and wrist-mounted D435). Right: Example multimodal observations (RGB images, point clouds, wrist views) and task objects used in real-world experiments.

achieves the lowest average smoothness score of 0.052, reducing the metric by 51.4%, 69.4%, and 77.2% relative to RDP, DP3, and Flow Policy, respectively. RDP exhibits lower smoothness than other diffusion-based baselines, indicating that latent action representations partially improve trajectory stability. However, its trajectories remain less smooth than those of LG-Flow Policy, as RDP does not impose explicit temporal smoothness constraints in the latent space. By contrast, LG-Flow Policy performs flow matching over temporally coherent latent trajectories, consistently suppressing high-frequency oscillations.

b) Task Success Rate and Response Time.: Table I summarizes task success rates and inference latency across simulated benchmarks. LG-Flow Policy achieves the highest average success rate of 78.3%, outperforming Flow Policy (+17.3%) and DP3 (+12.6%), and improving over RDP (73.0%) by 5.3%. While Flow Policy attains the lowest latency (6.1 ms), LG-Flow Policy incurs only a marginal increase (7.5 ms) and remains in the same real-time regime. Notably, LG-Flow Policy is approximately 7.5 \times faster than DP3 (55.9 ms), demonstrating a favorable success-latency trade-off with minimal loss in responsiveness.

Overall, simulation results show that LG-Flow Policy achieves a favorable trade-off among smooth execution, fast inference, and high task success, which is essential for real-time robotic manipulation.

C. Real-World Experiments

1) Real-World Experimental Setup:

a) Platform and Sensing.: Real-world experiments are conducted on a Franka Emika Panda arm with an interchangeable end-effector configuration, where the LEAP Hand can be replaced by a parallel gripper depending on the task (Fig. 5, left). A RealSense L515 global camera provides scene-level RGB-D observations, while a wrist-mounted RealSense D435 supplies local visual feedback. Both cameras operate at 640 \times 480 resolution and 30 fps. Depth images are converted to point clouds using calibrated intrinsics and extrinsics. In contrast to simulation, RGB images from the wrist-mounted camera are additionally used as execution-time conditioning inputs to the decoder, allowing low-level action realization to adapt to local visual variations during real-world execution.

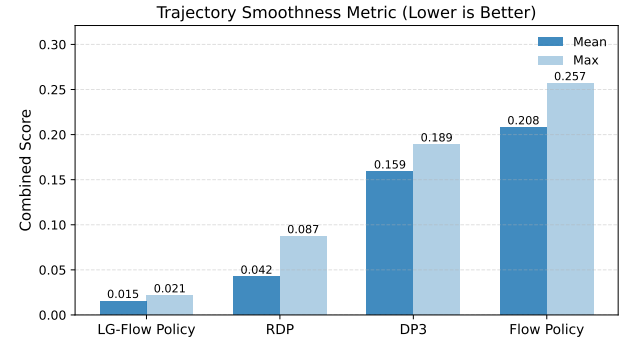


Fig. 6. Trajectory smoothness comparison across real-world manipulation tasks. Lower values indicate smoother execution.

b) Tasks.: We evaluate three real-world manipulation tasks: *pick-and-place*, performed with both the LEAP Hand and a parallel gripper to cover different manipulation modalities; *peg-in-hole*, which requires precise insertion; and *obstacle-avoidance grasping*, where a target object must be grasped while avoiding surrounding obstacles. Representative objects and environments are shown in Fig. 5 (top right).

c) Demonstrations and Baselines.: Expert demonstrations are collected via human teleoperation, with 30 demonstrations per task. We compare LG-Flow Policy against DP3 [3], Reactive Diffusion Policy (RDP) [13], and Flow Policy [9]. For RDP, tactile inputs are replaced with wrist camera images to ensure a fair comparison under visual-only settings.

d) Evaluation Protocol.: Each task is evaluated over 3 independent runs with different random seeds, each consisting of 10 trials (30 trials per task). Success rates are reported as mean \pm standard deviation. Response time measures end-to-end policy inference latency, excluding sensor acquisition and environment stepping. All experiments are conducted on identical hardware with an Intel Core i9-14900KF CPU and an NVIDIA RTX 4080 GPU.

2) Real-World Results Analysis: Quantitative real-world results are summarized in Table II and Fig. 6, evaluating trajectory smoothness, task success, and response time.

a) Trajectory Smoothness.: As shown in Fig. 6, LG-Flow Policy achieves the lowest mean and maximum smoothness scores among all methods, indicating substantially reduced

TABLE II

MAIN RESULTS FOR REAL-WORLD ROBOT EXPERIMENTS. SUCCESS RATES (%) ARE REPORTED AS MEAN \pm STANDARD DEVIATION OVER 30 TRIALS. AVG. SUCCESS DENOTES THE AVERAGE SUCCESS RATE ACROSS ALL TASKS. AVG. RESPONSE TIME MEASURES END-TO-END POLICY INFERENCE LATENCY PER CONTROL STEP.

Methods	Pick & Place	Pick & Place (Gripper)	Peg-in-Hole	Obstacle Avoidance	Avg. Success	Avg. Response Time
DP3	66.7 ± 5.8	80.0 ± 5.8	35.0 ± 5.8	50.0 ± 10.0	57.9	29.29 ms
RDP	73.3 ± 5.8	93.3 ± 5.8	50.0 ± 0.0	63.3 ± 5.8	70.0	31.82 ms
Flow Policy	60.0 ± 0.0	73.3 ± 5.8	30.0 ± 10.0	46.7 ± 5.8	52.5	6.54 ms
LG-Flow Policy (Ours)	83.3 ± 5.8	96.7 ± 5.8	60.0 ± 0.0	70.0 ± 5.8	77.5	8.59 ms

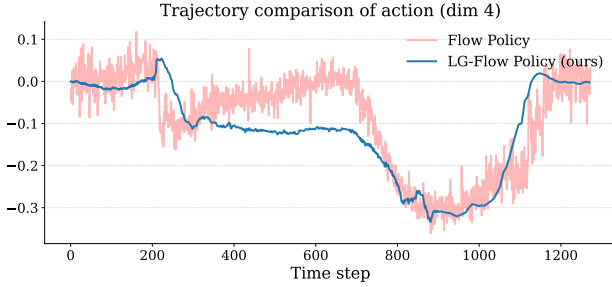


Fig. 7. Comparison of real-world joint trajectories under identical initial conditions. Flow Policy exhibits high-frequency oscillations and abrupt variations, while LG-Flow Policy generates smoother and more temporally coherent trajectories, consistent with the quantitative smoothness metrics.

jerk and high-frequency oscillations. Compared to Flow Policy, the mean smoothness metric is reduced by over 93.7%, demonstrating strong robustness under real-world sensing noise and actuation delays. Consistent with simulation results, RDP exhibits lower smoothness than other diffusion-based baselines, suggesting that latent action representations improve execution stability in physical settings. However, its trajectories remain less smooth than those of LG-Flow Policy, as RDP does not impose explicit temporal smoothness constraints in the latent space.

This effect is further illustrated in Fig. 7, where Flow Policy produces pronounced high-frequency oscillations, while LG-Flow Policy yields smooth and temporally coherent joint motions under identical initial conditions.

b) Task Success Rate and Response Time.: Table II reports task success rates and inference latency in real-world experiments. LG-Flow Policy achieves the highest average success rate of 77.5%, outperforming DP3 (57.9%), RDP (70.0%), and Flow Policy (52.5%). While Flow Policy attains the lowest latency (6.54 ms), its unstable trajectories often lead to execution failures. LG-Flow Policy incurs only a modest increase in response time (8.59 ms) while achieving substantially higher task success. One contributing factor to the improved success of both RDP and LG-Flow Policy is the incorporation of wrist-mounted camera observations during action decoding, providing execution-time visual feedback for precise manipulation. LG-Flow Policy remains over 3× faster than DP3 and RDP, indicating that significant real-world performance gains are achieved at minimal computational cost.

Overall, real-world results confirm that LG-Flow Policy strikes a robust balance between inference efficiency, trajectory smoothness, and task success, supporting its suitability for

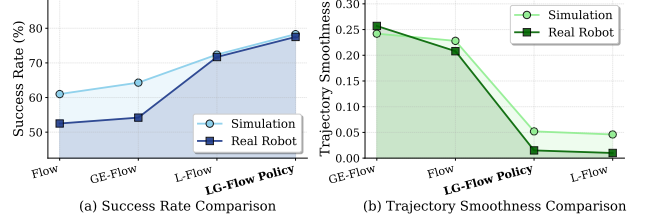


Fig. 8. Ablation study on trajectory smoothness and task success rate in real world manipulation tasks.

stable real-world deployment.

D. Ablation Study

Fig. 8 summarizes ablation results in both simulation and real-world settings, analyzing the contributions of geometry-aware perception (GE-Flow) and latent action modeling (L-Flow). Across both domains, the two components exhibit complementary effects on task success and trajectory smoothness.

In simulation, geometry-aware encoding improves average success from 61% to 64.3% but slightly degrades trajectory smoothness, indicating that enhanced spatial perception alone does not resolve temporal instability. In contrast, latent action modeling substantially reduces the smoothness metric (0.228 \rightarrow 0.046) while increasing success to 72.4%. Combining both components further improves success to 78.3% while maintaining low oscillations.

A similar trend is observed in real-world experiments. While geometry-aware perception alone yields only marginal success gains (52.5% \rightarrow 54.2%), it noticeably increases trajectory oscillations, often leading to execution failures under real-world noise and actuation delays. Latent action modeling, by contrast, improves both metrics, increasing success to 71.7% and reducing smoothness by over 95%. Combining both components achieves the best real-world performance, reaching a success rate of 77.5% with minimal oscillations.

Overall, these results indicate that geometry-aware perception enhances spatial understanding, whereas stable manipulation critically relies on enforcing temporal coherence through latent action modeling, particularly in real-world settings.

V. CONCLUSION

This work addresses real-time robotic manipulation under long-horizon and high-dimensional control, where existing generative policies struggle to jointly achieve expressive behavior modeling, fast inference, and stable execution, limiting their deployment on physical systems.

We propose **LG-Flow Policy**, a trajectory-level action generation framework that performs flow matching in a continuous latent action space. By mapping action sequences into a temporally regularized latent trajectory manifold and learning an explicit latent-space flow, LG-Flow Policy enables near single-step inference while substantially improving execution smoothness and stability. Operating on motion-level latent representations decouples global trajectory structure from low-level control noise, mitigating error amplification during generation and leading to more reliable long-horizon behaviors.

LG-Flow Policy further integrates geometry-aware point cloud conditioning and execution-time decoding modulation, allowing additional sensory signals to be incorporated without perturbing latent trajectory dynamics. This design enables richer multimodal execution while preserving fast response, as demonstrated by visual-conditioned decoding with a wrist-mounted camera in real-world experiments. Extensive simulation and real-robot results show smooth trajectories, high success rates, and rapid inference, outperforming both diffusion-based and raw action-space flow-based baselines.

Despite its effectiveness, the current system adopts relatively lightweight multimodal fusion and does not explicitly model complex contact dynamics. Future work will explore richer multimodal representations and contact-aware latent dynamics to extend LG-Flow Policy toward more challenging contact-rich manipulation.

REFERENCES

- [1] C. Chi, Z. Xu, S. Feng, E. Cousineau, Y. Du, B. Burchfiel, R. Tedrake, and S. Song, “Diffusion policy: Visuomotor policy learning via action diffusion,” *The International Journal of Robotics Research*, vol. 44, no. 10-11, pp. 1684–1704, 2025.
- [2] Z. Ni, Y. He, L. Qian, J. Mao, F. Fu, W. Sui, H. Su, J. Peng, Z. Wang, and B. He, “Vo-dp: Semantic-geometric adaptive diffusion policy for vision-only robotic manipulation,” *arXiv preprint arXiv:2510.15530*, 2025.
- [3] Y. Ze, G. Zhang, K. Zhang, C. Hu, M. Wang, and H. Xu, “3d diffusion policy: Generalizable visuomotor policy learning via simple 3d representations,” in *Proceedings of Robotics: Science and Systems (RSS)*, 2024.
- [4] C. Wang, H. Shi, W. Wang, R. Zhang, L. Fei-Fei, and C. K. Liu, “Dexcap: Scalable and portable mocap data collection system for dexterous manipulation,” *arXiv preprint arXiv:2403.07788*, 2024.
- [5] D. Wang, C. Liu, F. Chang, and Y. Xu, “Hierarchical diffusion policy: manipulation trajectory generation via contact guidance,” *IEEE Transactions on Robotics*, 2025.
- [6] Y. Lipman, R. T. Chen, H. Ben-Hamu, M. Nickel, and M. Le, “Flow matching for generative modeling,” *arXiv preprint arXiv:2210.02747*, 2022.
- [7] R. T. Chen and Y. Lipman, “Flow matching on general geometries,” *arXiv preprint arXiv:2302.03660*, 2023.
- [8] S. Fotiadis, N. D. Brenowitz, T. Geffner, Y. Cohen, M. Pritchard, A. Vahdat, and M. Mardani, “Adaptive flow matching for resolving small-scale physics,” in *Forty-second International Conference on Machine Learning*.
- [9] Q. Zhang, Z. Liu, H. Fan, G. Liu, B. Zeng, and S. Liu, “Flowpolicy: Enabling fast and robust 3d flow-based policy via consistency flow matching for robot manipulation,” in *Proceedings of the AAAI Conference on Artificial Intelligence*, vol. 39, no. 14, 2025, pp. 14 754–14 762.
- [10] H. Ding, N. Jaquier, J. Peters, and L. Rozo, “Fast and robust visuomotor riemannian flow matching policy,” *IEEE Transactions on robotics*, 2025.
- [11] M. Braun, N. Jaquier, L. Rozo, and T. Asfour, “Riemannian flow matching policy for robot motion learning. in 2024 ieee,” in *RSJ International Conference on Intelligent Robots and Systems (IROS)*, pp. 5144–5151.
- [12] Y. Ze, Z. Chen, W. Wang, T. Chen, X. He, Y. Yuan, X. B. Peng, and J. Wu, “Generalizable humanoid manipulation with 3d diffusion policies,” in *2025 IEEE/RSJ International Conference on Intelligent Robots and Systems (IROS)*. IEEE, 2025, pp. 2873–2880.
- [13] H. Xue, J. Ren, W. Chen, G. Zhang, Y. Fang, G. Gu, H. Xu, and C. Lu, “Reactive diffusion policy: Slow-fast visual-tactile policy learning for contact-rich manipulation,” in *Proceedings of Robotics: Science and Systems (RSS)*, 2025.
- [14] J. Ho, A. Jain, and P. Abbeel, “Denoising diffusion probabilistic models,” *Advances in neural information processing systems*, vol. 33, pp. 6840–6851, 2020.
- [15] J. Song, C. Meng, and S. Ermon, “Denoising diffusion implicit models,” *arXiv preprint arXiv:2010.02502*, 2020.
- [16] P. Florence, C. Lynch, A. Zeng, O. A. Ramirez, A. Wahid, L. Downs, A. Wong, J. Lee, I. Mordatch, and J. Tompson, “Implicit behavioral cloning,” in *Conference on robot learning*. PMLR, 2022, pp. 158–168.
- [17] K. He, X. Zhang, S. Ren, and J. Sun, “Deep residual learning for image recognition,” in *Proceedings of the IEEE conference on computer vision and pattern recognition*, 2016, pp. 770–778.
- [18] A. Dosovitskiy, L. Beyer, A. Kolesnikov, D. Weissenborn, X. Zhai, T. Unterthiner, M. Dehghani, M. Minderer, G. Heigold, S. Gelly, J. Uszkoreit, and N. Houlsby, “An image is worth 16x16 words: Transformers for image recognition at scale,” *ICLR*, 2021.
- [19] A. Goyal, J. Xu, Y. Guo, V. Blukis, Y.-W. Chao, and D. Fox, “Rvt: Robotic view transformer for 3d object manipulation,” in *Conference on Robot Learning*. PMLR, 2023, pp. 694–710.
- [20] R. Wang, J. Zhang, J. Chen, Y. Xu, P. Li, T. Liu, and H. Wang, “Dexgraspnet: A large-scale robotic dexterous grasp dataset for general objects based on simulation,” *arXiv preprint arXiv:2210.02697*, 2022.
- [21] J. Zhang, H. Liu, D. Li, X. Yu, H. Geng, Y. Ding, J. Chen, and H. Wang, “Dexgraspnet 2.0: Learning generative dexterous grasping in large-scale synthetic cluttered scenes,” in *8th Annual Conference on Robot Learning*, 2024.
- [22] C. R. Qi, H. Su, K. Mo, and L. J. Guibas, “Pointnet: Deep learning on point sets for 3d classification and segmentation,” in *Proceedings of the IEEE conference on computer vision and pattern recognition*, 2017, pp. 652–660.
- [23] D. Turpin, T. Zhong, S. Zhang, G. Zhu, E. Heiden, M. Macklin, S. Tsogkas, S. Dickinson, and A. Garg, “Fast-grasp’d: Dexterous multi-finger grasp generation through differentiable simulation,” in *ICRA*, 2023.
- [24] A. Van Den Oord, O. Vinyals *et al.*, “Neural discrete representation learning,” *Advances in neural information processing systems*, vol. 30, 2017.
- [25] J. Bjorck, F. Castañeda, N. Cherniadev, X. Da, R. Ding, L. Fan, Y. Fang, D. Fox, F. Hu, S. Huang *et al.*, “Gr00t n1: An open foundation model for generalist humanoid robots,” *arXiv preprint arXiv:2503.14734*, 2025.
- [26] J. Bruce, M. D. Dennis, A. Edwards, J. Parker-Holder, Y. Shi, E. Hughes, M. Lai, A. Mavalankar, R. Steigerwald, C. Apps *et al.*, “Genie: Generative interactive environments,” in *Forty-first International Conference on Machine Learning*, 2024.
- [27] Q. Bu, J. Cai, L. Chen, X. Cui, Y. Ding, S. Feng, X. He, X. Huang *et al.*, “Agibot world colosseo: A large-scale manipulation platform for scalable and intelligent embodied systems,” in *2025 IEEE/RSJ International Conference on Intelligent Robots and Systems (IROS)*. IEEE, 2025.
- [28] S. Gao, S. Zhou, Y. Du, J. Zhang, and C. Gan, “Adaworld: Learning adaptable world models with latent actions,” in *International Conference on Machine Learning (ICML)*, 2025.
- [29] A. Liang, P. Czempin, M. Hong, Y. Zhou, E. Biyik, and S. Tu, “Clam: Continuous latent action models for robot learning from unlabeled demonstrations,” *arXiv preprint arXiv:2505.04999*, 2025.
- [30] J. Yang, Y. Shi, H. Zhu, M. Liu, K. Ma, Y. Wang, G. Wu, T. He, and L. Wang, “Como: Learning continuous latent motion from internet videos for scalable robot learning,” *arXiv preprint arXiv:2505.17006*, 2025.
- [31] A. Nikulin, I. Zisman, D. Tarasov, N. Lyubaykin, A. Polubarov, I. Kiselev, and V. Kurenkov, “Latent action learning requires supervision in the presence of distractors,” in *International Conference on Machine Learning (ICML)*, 2025.
- [32] A. Rajeswaran, V. Kumar, A. Gupta, G. Vezzani, J. Schulman, E. Todorov, and S. Levine, “Learning complex dexterous manipulation with deep reinforcement learning and demonstrations,” *arXiv preprint arXiv:1709.10087*, 2017.
- [33] T. Yu, D. Quillen, Z. He, R. Julian, K. Hausman, C. Finn, and S. Levine, “Meta-world: A benchmark and evaluation for multi-task and meta reinforcement learning,” in *Conference on robot learning*. PMLR, 2020, pp. 1094–1100.
- [34] E. Todorov, T. Erez, and Y. Tassa, “Mujoco: A physics engine for model-based control,” in *2012 IEEE/RSJ international conference on intelligent robots and systems*. IEEE, 2012, pp. 5026–5033.